

# Local Structure of the Impurity Site in Nd:LaF<sub>3</sub> by X-Ray Fluorescence Holography

Jens Rüdiger Stellhorn,\* Shinya Hosokawa, Naohisa Happo, Kouichi Hayashi, Tomohiro Matsushita, Noriaki Kawaguchi, and Takayuki Yanagida

The local structure around the dopant atom in Nd(8 mol%):LaF<sub>3</sub> single-crystal scintillator is analyzed by X-ray fluorescence holography experiments in combination with a sparse modeling algorithm. The average local environment of Nd is reconstructed up to large distances of about 12 Å and confirms a substitution of La atoms with Nd with only small crystal lattice distortions. The experimental findings are substantiated by comparison with reference data from La holograms and with computationally generated holograms based on a model structure of the dopant site.

## 1. Introduction

The determination of the local structure around impurity sites in a crystal matrix is a formidable task for the structural characterizations of complex functional materials. If the impurity atoms are randomly distributed, they lack the long-range periodicity needed for the usual diffraction experiments, which still represents the standard method for crystallography. This is a serious drawback for state-of-the-art investigations, as many functions can only be achieved by doping, and experimental verification of structural models is highly desirable. X-ray fluorescence holography (XFH) is a versatile and powerful method that can be applied for this task.<sup>[1]</sup>

XFH is a powerful tool to investigate such atomic positions and their positional fluctuations around a specific constituent


element.<sup>[2]</sup> The technique is based on the angular dependence of X-ray fluorescence intensity from an emitter atom caused by an X-ray standing wavefield, which is formed by the interference of an incident X-ray wave (reference wave) with the X-rays scattered from nearby atoms (object wave).<sup>[2,3]</sup> The variation of X-ray fluorescence intensity is in the order of magnitude of some 0.1%. From this experimentally accessible data, 3D atomic images can be obtained by a Fourier transform-like

algorithm. The reconstructions can be further improved by a sparse-modeling approach for the reconstruction.<sup>[1]</sup> This technique is suitable for determining impurity sites and their local environments, which cannot be easily detected by usual diffraction methods.

Prominent recent examples where XFH was used to investigate the impurity site are the characterization of lattice distortions around Ga impurity atoms in InSb single crystals,<sup>[4]</sup> the determination of the spontaneous formation of suboxidic coordination around Co in ferromagnetic rutile,<sup>[5]</sup> the determination of different dopant sites in topological insulators like Mn:Bi<sub>2</sub>Te<sub>3</sub><sup>[6]</sup> and In:Bi<sub>2</sub>Se<sub>3</sub>,<sup>[7]</sup> the atomic environment around Ca cations in a doped KTaO<sub>3</sub> wafer,<sup>[8]</sup> or studying the effect of heavy element doping of Ta in a Fe<sub>2</sub>VAl Heusler-type

Dr. J. R. Stellhorn  
Department of Applied Chemistry  
Hiroshima University  
Higashihiroshima 739-8527, Japan  
E-mail: stellhoj@hiroshima-u.ac.jp

Dr. J. R. Stellhorn  
Photon Science  
Deutsches Elektronen-Synchrotron (DESY)  
Hamburg 22607, Germany

 The ORCID identification number(s) for the author(s) of this article can be found under <https://doi.org/10.1002/pssb.202000310>.

© 2020 The Authors. Published by WILEY-VCH Verlag GmbH & Co. KGaA, Weinheim. This is an open access article under the terms of the Creative Commons Attribution-NonCommercial License, which permits use, distribution and reproduction in any medium, provided the original work is properly cited and is not used for commercial purposes.

The copyright line for this article was changed on 9 September 2020 after original online publication.

Correction added on 4 September 2020, after first online publication: Projekt Deal funding statement has been added.

DOI: 10.1002/pssb.202000310

Prof. S. Hosokawa  
Department of Physics  
Kumamoto University  
Kumamoto 860-8555, Japan

Prof. N. Happo  
Graduate School of Information Sciences  
Hiroshima City University  
Hiroshima 731-3194, Japan

Prof. K. Hayashi  
Department of Physical Science and Engineering  
Nagoya Institute of Technology  
Nagoya 466-8555, Japan

Prof. T. Matsushita  
Japan Synchrotron Radiation Research Institute (JASRI)  
Sayo 679-5198, Japan

Prof. T. Matsushita, Prof. N. Kawaguchi, Prof. T. Yanagida  
Division of Materials Science  
Nara Institute of Science and Technology (NAIST)  
Ikoma 630-0192, Japan

thermoelectric material.<sup>[9]</sup> XFH is, however, not limited to impurities, but can also be useful for the investigation of bulk samples, in particular for chalcogenide superconductors<sup>[10]</sup> and also in general for determining positional fluctuations of atoms.<sup>[11–13]</sup>

In this study, we use XFH to examine the structure of Nd impurities in a highly doped Nd:LaF<sub>3</sub> single crystal. Due to its strong emission in the vacuum ultraviolet (VUV) region, Nd-doped LaF<sub>3</sub> is an interesting scintillator for applications in  $\gamma$ -ray detectors and for fluorescence bioimaging.<sup>[14,15]</sup> The scintillating efficiency increases proportionally with Nd concentration up to a saturated level of about 10 mol% NdF<sub>3</sub>.<sup>[16,17]</sup> Recently, pure and heavily doped Nd:LaF<sub>3</sub> single crystals were successfully prepared and were shown to exhibit a high light-yield and VUV emission intensity.<sup>[14,18]</sup> Furthermore, Nd:LaF<sub>3</sub> is of interest for spectroscopic investigations, e.g., concerning cooperative quantum states of Nd ion pairs.<sup>[19,20]</sup> To understand the remarkable properties of Nd:LaF<sub>3</sub>, it is important to clarify the position of the dopant in the host lattice and the extent of local lattice distortions around it.

## 2. Experimental Section

We investigated Nd:LaF<sub>3</sub> single-crystal sample with a NdF<sub>3</sub> content of about 8 mol%. The crystal was grown in a vacuum-tight Czochralski system equipped with a radio frequency induction heater and an automatic diameter control system. The crucible and thermal insulators were made of high-purity graphite. As starting materials, commercial fluoride powders of LaF<sub>3</sub> and NdF<sub>3</sub> (purity >99.99%) were prepared and loaded into the graphite crucible, with NdF<sub>3</sub> starting concentration of 10 mol%. The sample was preheated under vacuum to eliminate water and oxygen traces from the growth chamber and the starting materials. Subsequently, high-purity CF<sub>4</sub>/Ar gas was introduced into the furnace. Then, the starting material was melted and the crystal was pulled up along the *c*-axis direction using an undoped LaF<sub>3</sub> seed crystal. The crystallinity of the sample was characterized by X-ray rocking curve analysis using a Bruker AXS D8 Discover system. The distribution of Nd in the crystal was checked by energy-dispersive X-ray analysis using a Bruker AXS Quantax system with an XFlash detector, and the final Nd content was determined to be around 8 mol%. Further details on the sample characteristics are outlined in a previous study.<sup>[14]</sup>

Multienery XFH experiments were conducted at eight incident energies above the Nd *L*<sub>1</sub> absorption edge (7.126 keV). The measurements were carried out at the beamline BL39XU of the SPring-8 at room temperature. We used the inverse mode of XFH by rotating two angles of the sample, the incident angle of  $0^\circ \leq \theta \leq 75^\circ$  in steps of  $1.00^\circ$  and the azimuthal angle of  $0^\circ \leq \phi \leq 360^\circ$  in steps of  $0.30^\circ$ . Nd *L* <sub>$\gamma$</sub>  fluorescent X-rays (6.602 keV) were collected using a silicon drift detector via a cylindrical graphite crystal energy analyzer. The *L* <sub>$\gamma$</sub>  line of Nd was chosen to avoid interference of the La fluorescence lines, which cannot be resolved from Nd *L* <sub>$\alpha$</sub>  and *L* <sub>$\beta$</sub> . The XFH signals were recorded at eight different incident energies between 7.2 and 10.5 keV.

Additional holograms were measured for the La *L* <sub>$\alpha$</sub>  (4.650 keV) fluorescence line at the beamline BL12B2 of the SPring-8 under the same conditions. Due to the lower

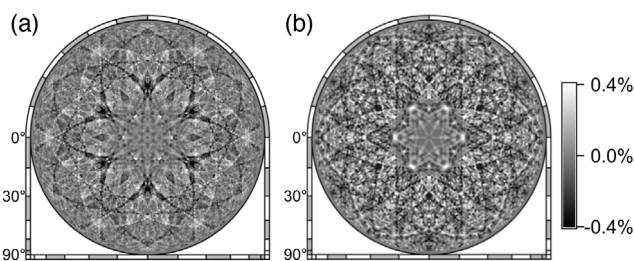


**Figure 1.** Exemplary experimental holograms of Nd:LaF<sub>3</sub>. a) For Nd *L* <sub>$\gamma$</sub>  at 7.5 keV and b) for La *L* <sub>$\alpha$</sub>  at 10.5 keV.

X-ray intensity at this experimental station and the lower energy of the fluorescence line, the La holograms have a slightly worse statistical quality than the Nd holograms but are still well suitable as reference data. Further details on the XFH method and its implementation can be found in previous studies.<sup>[2,3,21]</sup>

Exemplary experimental holograms for Nd and La are shown in Figure 1a,b in an orthographic projection. The intensity scale indicates the variation of the fluorescence intensity relative to the averaged value. The holograms are centered at  $\theta = 0^\circ$ , and the radial and angular directions indicate  $\theta$  and  $\phi$ , respectively.

## 3. Data Analysis

The X-ray fluorescence holograms can be used to reconstruct the local atomic environments in real space. For this purpose, we used a scattering pattern matrix extraction algorithm with *L*<sub>1</sub> regularized linear regression (SPEA-L1).<sup>[22,23]</sup> The SPEA-L1 algorithm represents a sparse modeling approach to the experimental data.<sup>[24]</sup> The parameters for the SPEA-L1 calculations were set as follows. The sparseness of the atomic reconstruction is controlled by the parameter  $\lambda$ , which was set to  $\lambda = \beta \cdot \max(-\partial E(g)/\partial g)$ , where  $E(g)$  is the mean error function and  $g$  is the voxel value of the atomic image.<sup>[23]</sup> The parameter  $\beta$  was set to be 0.9. The real space was reconstructed in a 12 Å radius around the emitter atom with a voxel size of  $0.1 \times 0.1 \times 0.1 \text{ Å}^3$ .

For comparison with the experimental data, we also consider a model of Nd:LaF<sub>3</sub> and calculated the holograms from this

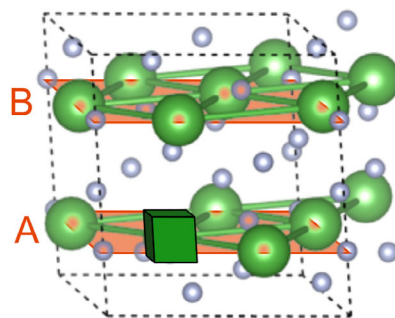


**Figure 2.** 3D model of the crystal unit cell (indicated by the dashed lines) of LaF<sub>3</sub>, with one La atom chosen as the emitter atom (indicated as green cube) that defines the two different layers A (containing the emitter atom) and B (above the emitter atom). Image created with VESTA.<sup>[25]</sup>

structure. The model is based on the crystal unit cell of pure  $\text{LaF}_3$ , as shown in **Figure 2**. The crystal lattice consists of two ABAB stacked hexagonal layers of La atoms, with each La atom being coordinated additionally by 9 F atoms. The space group is  $P\bar{3}c1$  with lattice parameters of  $a = 7.26 \text{ \AA}$  and  $c/a = 1.023$ . There are six  $\text{LaF}_3$  units in the unit cell.<sup>[26]</sup> For the  $\text{Nd}:\text{LaF}_3$  model, a large  $10 \times 10 \times 10$  supercell of the crystal lattice was generated, and 1 La atom was exchanged with Nd (example indicated for the unit cell in **Figure 2** with the green cube). A subsequent symmetrization of the data with the crystal symmetry parameters produces a superposition of all different relative orientations (see below). The holograms were calculated for the Nd emitter at the same incident X-ray energies as for the experimental data. For better comparability, the computationally generated holograms were also subjected to a similar background removal treatment as the experimental data and were also limited in the range of the experimental exit angle to  $0^\circ \leq \theta \leq 75^\circ$ . Exemplary holograms are shown in **Figure 3**. The features of the experimental (**Figure 1**) and computational holograms (**Figure 3**) are in good agreement, for example, considering the intense line-like features (X-ray standing wavelines).

## 4. Results and Discussion

The result of real-space reconstruction from the X-ray fluorescence holograms is the average local structure around the emitter atom. A first view on the structure is shown in **Figure 4** by 3D reconstruction. The figure compares directly the space of the first neighbors around La (i.e., reconstructed from the  $\text{La } L_\alpha$  holograms) and the Nd atoms (i.e. reconstructed from the

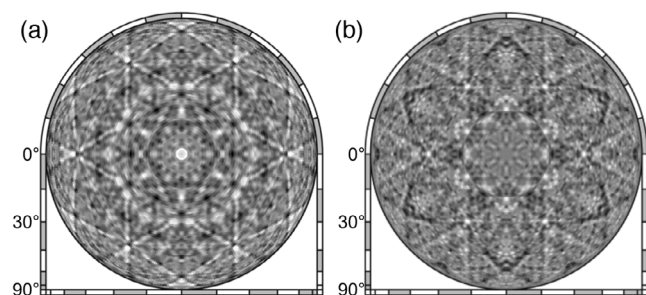


**Figure 3.** Exemplary computationally generated holograms of  $\text{Nd}:\text{LaF}_3$ . a) For Nd at 7.5 keV and b) for La at 10.5 keV.

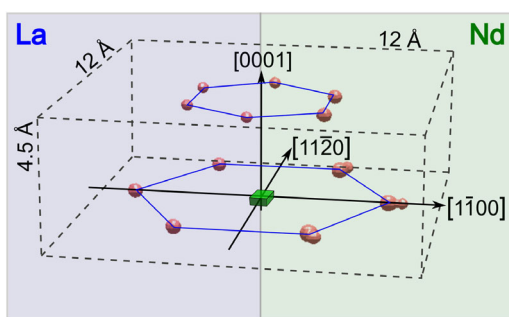


**Figure 4.** Comparison of the 3D reconstruction of the local environment of the La (left) and Nd (right) emitter atoms (indicated as green cube).

Nd  $L_\gamma$  holograms). The 3D reconstructions show hexagonally distributed atomic images in two planes (corresponding to the A and B plane) with a similar intensity and location for the La and Nd reconstructions. An unexpected feature is the “tail” visible in the radial direction beyond some of the in-plane neighbors of Nd (which will be discussed later).

To understand these signals, the average structure in the La planes should be considered, as shown in **Figure 5**. The hexagonal distribution of the atomic images in the plane of the emitter atom shown in **Figure 4** corresponds to the nearest La sites in **Figure 5a**. Note that there are two different La–La distances in the crystal structure, which are represented with green bars (shorter bonds) and dashed green lines (longer bonds) and have a difference of about  $0.13 \text{ \AA}$ . If the Nd atom is randomly distributed at the La positions, then the average structure is a symmetrical mixture of the longer and shorter bonds. Also, as shown in **Figure 5b**, the atomic images reconstructed from XFH in the B plane are a mix of La and F sites, with a site occupancy of  $1/2$  La and  $1/2$  F atoms (see the blue hexagons indicating the neighbor positions), which explains the lower intensity of the upper atomic images in **Figure 4**. Overall, the features of 3D XFH reconstruction matches well with the average structure expected from Nd substitution of the La sites.

A large 2D slice with an area of  $24 \times 24 \text{ \AA}^2$  through the A plane containing the emitter atom is shown in **Figure 6**. The experimental result for the Nd environment is shown in (a), where the first- and third-nearest La neighbors are well visible, whereas the second and fourth in-plane La neighbors have lower intensities. For better visibility, the region of the fourth-nearest neighboring La atoms was magnified by a factor of 10 in intensity. See the schematic view of the average structure in (b) for the indication of the  $i$ th neighbor. Furthermore, no pure images of the F atoms can be distinguished in the experimental reconstruction. This is a result of the low number of electrons of F compared with the much heavier lanthanides, and the low occupation numbers in the average structure (only  $1/2$  for the F sites in **Figure 6b**).

For reference, the reconstruction from the experimental La holograms and from the computationally generated holograms

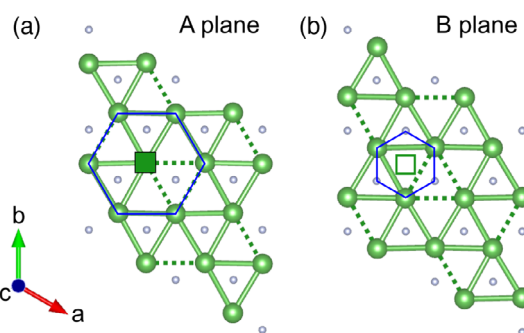


**Figure 5.** Model of the La planes in  $\text{LaF}_3$  perpendicular to the  $[0001]$  direction, extended to  $2 \times 2$  unit cells. a) A slice of the A plane containing the emitter atom (shown as green square), and b) a slice of the B plane, where the relative location of the emitter atom is indicated by the empty green square. The positions of the nearest La sites are illustrated by the blue hexagons. Short and long La–La bonds are indicated with green bars and dashed lines, respectively.

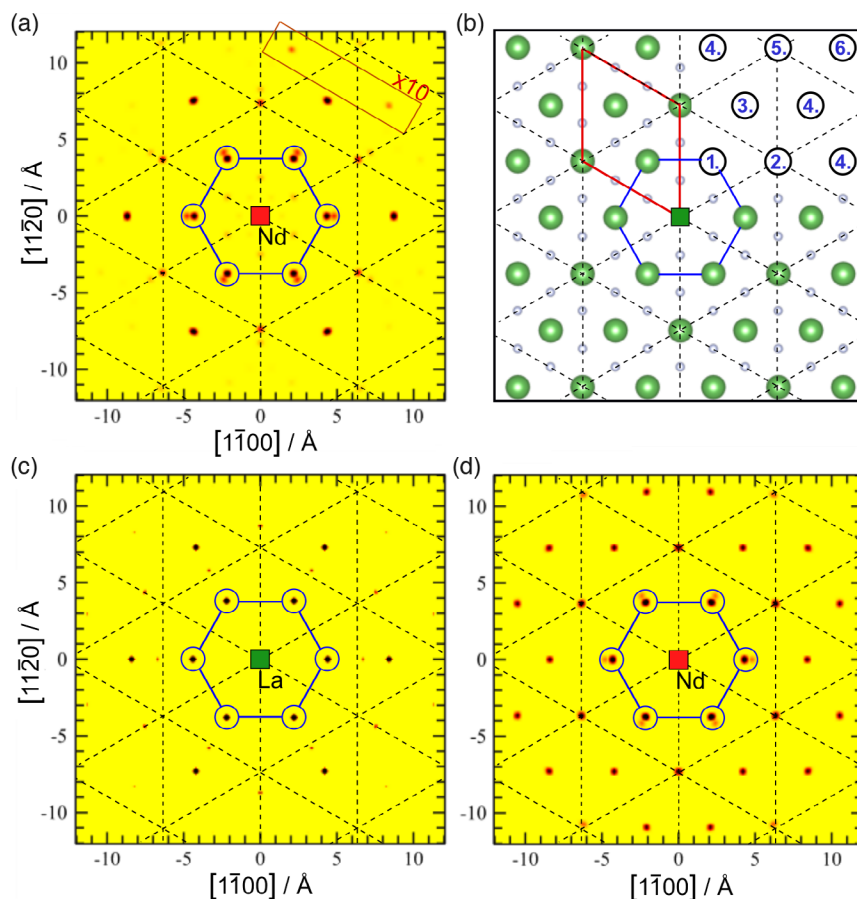


**Figure 6.** The A plane containing the emitter atom (illustrated as red [Nd] and green [La] square). a) Reconstruction from the Nd holograms (in the marked region, the intensity scale was magnified by a factor of 10), b) schematic view of the average structure of this plane (with the size of the crystal unit cell indicated by the red marked rhombus, and the  $i$ th in-plane La neighbor atom indicated by the blue numbers), c) reconstruction from the La holograms (reference data), and d) reconstruction from the computationally generated data for the model of Nd:LaF<sub>3</sub>. The dashed lattice corresponds to the averaged crystal lattice, and the blue hexagons indicate the first La neighbors of the emitter atom.

of the Nd:LaF<sub>3</sub> model is shown in Figure 6c,d, respectively. The similar location of the atomic images in the averaged crystal lattice (dashed lines) confirms that Nd substitutes La in the crystal lattice and verifies the size of the unit cell. Concerning the intensity distribution of the images, it should be noted that image intensities in XFH in general depend on various factors, notably atomic positional fluctuations and the distance from the emitter atom, but are also subject to XFH-specific effects, like the twin-image problem or limited angular or energy ranges for the input data.<sup>[2]</sup> The agreement between the trends of intensities for Nd emitters and the La reference in (a) and (b) (lower intensities of the second and fourth in-plane La neighbors) suggests that these are rather connected to the latter effects. It may also be noted that the distance of the fourth neighbor is comparably large with already 12.6 Å. The even lower visibility of the signals in the La reconstructions in (b) is related to the lower statistical quality of the La  $L_{\alpha}$  holograms (see Section 2).

The result for the reconstruction from the holograms that were generated computationally from the Nd LaF<sub>3</sub> model is shown in Figure 6d. All signals corresponding to the La sites as seen in (b) are visible, and the distance depending on the

image intensities agrees well with the experimental data of both Nd and La. Furthermore, a tail in the radial direction beyond the first neighboring La atom is observed, similar to the case in (a), confirming that this feature is caused by the interference of the signals of the two La sites with slightly different distances.

The La plane above the emitter atom with  $z = 3.6$  Å (B plane) is shown in Figure 7. The experimental result of the Nd atoms is shown in (a). Only the first neighboring La atoms and a weak signal at the position of the second in-plane neighbor at a distance of about 4.9 Å from the origin as well as a strong signal at the position of the fifth in-plane neighbor (at a distance of about 9.8 Å) are observed. For the determination of the  $i$ th neighbor site, again a schematic slice of the average structure of this plane is shown in (b). Note that all sites are occupied by 1/2 La and 1/2 F atoms. The trend of the relative image intensities can be understood when compared with the reference data for La atoms in (c) and for the computationally generated data in (d). The La reconstruction in (b) confirms the same location of the atomic images for both Nd and La emitters, but it lacks images for the farther sites. This can again again



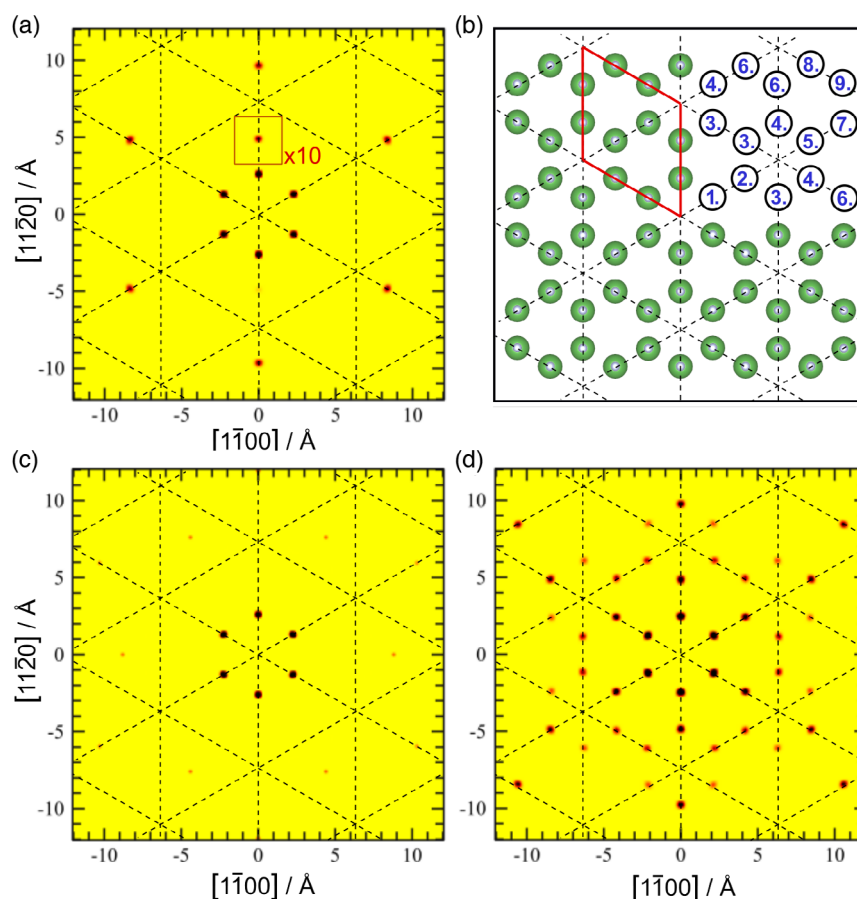


**Figure 7.** The B plane (above the emitter atom). a) Reconstruction from the Nd holograms (in the marked region, the intensity scale was magnified by a factor of 10), b) schematic view of the average structure of this plane (with the size of the crystal unit cell indicated by the red marked rhombus and the  $i$ th in-plane La neighbor atom indicated by the blue numbers), c) reconstruction from the La holograms (reference data), and d) reconstruction from the computationally generated data for the model of Nd:LaF<sub>3</sub>.

be explained by the lower statistical quality of the La holograms. On the other hand, the computational results in (d) again confirm the location of the atomic images and can also explain the trend of the visibility of the images in (a), as the fifth in-plane neighbor site exhibits a relatively strong image. The other signals in the experimental reconstructions are too weak to be observed, which is probably related to positional fluctuations of the distant atoms. Such fluctuations can affect the image intensity in XFH even when the induced displacements are smaller than the spatial resolution of the method, see details outlined in a previous study.<sup>[4]</sup>

Overall, the features of the experimental and computational reconstructions confirm that Nd replaces La in the crystal lattice and that substitution leads to only very small lattice distortions. A number of studies on Nd:LaF<sub>3</sub> implicitly assume this kind of substitutional position of the impurity atom (e.g., previous studies<sup>[27,28]</sup>), but here we present the first experimental evidence. It may be noted that although chemical arguments support this assumption, current results especially by XFH investigations show that the situation is not necessarily always so trivial, as was shown for example in the case of Mn:Bi<sub>2</sub>Te<sub>3</sub>, where two impurity sites coexist,<sup>[6]</sup> though extended X-ray

spectroscopy investigations (EXAFS) favored a purely interstitial position.<sup>[29]</sup>

As discussed in the introduction, the structural information gained by XFH is not available from other techniques: X-ray diffraction cannot determine information on the (randomly distributed) impurity position; while EXAFS could, in principle, provide information on the local environment around Nd atoms, it is highly complicated by the comparably large distances of more than 4 Å of even the first La neighboring atoms and the fact that EXAFS only contains 1D information, whereas several sites with similar distances exist in this crystal in different layers. On the other hand, XFH provides clear atomic images in 3D up to distances of about 12 Å. The reconstructions demonstrate the outstanding potential of XFH to obtain 3D information on the local structure in a large spatial range. Furthermore, the good agreement between experimental data for the Nd and La emitters and the computationally generated model demonstrate that no significant lattice distortions take place around the dopant site. In the light of previous XFH characterizations of the local structure around dopant sites (examples are given in previous studies<sup>[5–9]</sup>), this is a rather unusual situation and may be explained by the stability of the

LaF<sub>3</sub> lattice and the same oxidization state of the lanthanides (nominally Nd<sup>3+</sup> and La<sup>3+</sup>).

## 5. Conclusion

XFH analysis of the local structure around Nd dopants in LaF<sub>3</sub> revealed experimentally that Nd replaces La in the crystal lattice. The visualization of 3D and element-specific local structures is a unique advantage of XFH compared with other experimental techniques. Atomic images up to large distances of about 12 Å are well reconstructed. The substitution induces only minimal lattice distortions, which are shown by the good agreement between the experimental reconstructions of the local environment around La and Nd atoms and the results from a computationally generated model.

## Acknowledgements

The XFH experiments were conducted at BL39XU (exp. no: 2017A1227) and at BL12B2 (exp. no: 2018A4134) at SPring-8, Japan. This work was supported by the Japan Society for the Promotion of Science (JSPS) Grant-in-Aid for Scientific Research on Innovative Areas '3D Active-Site Science' (nos. 26105006 and 26105013). JRS gratefully acknowledges financial support as researcher under a postdoctoral fellowship of the Alexander-von-Humboldt foundation. Open access funding enabled and organized by Projekt DEAL.

## Conflict of Interest

The authors declare no conflict of interest.

## Keywords

impurity sites, LaF<sub>3</sub>, local structure, Nd dopant, scintillators, X-ray fluorescence holography

Received: June 9, 2020

Revised: July 3, 2020

Published online: July 21, 2020

- [1] S. Hosokawa, J. R. Stellhorn, K. Hayashi, T. Matsushita, *Phys. Status Solidi B* **2018**, 255, 1800089.
- [2] K. Hayashi, N. Happe, S. Hosokawa, W. Hu, T. Matsushita, *J. Phys.: Condens. Matter* **2012**, 24, 093201.
- [3] M. Tegze, G. Faigel, *Nature* **1996**, 380, 49.
- [4] S. Hosokawa, N. Happe, T. Ozaki, H. Ikemoto, T. Shishido, K. Hayashi, *Phys. Rev. B* **2013**, 87, 094104.
- [5] W. Hu, K. Hayashi, T. Fukumura, K. Akagi, M. Tsukada, N. Happe, S. Hosokawa, K. Ohwada, M. Takahashi, M. Suzuki, M. Kawasaki, *Appl. Phys. Lett.* **2015**, 106, 222403.
- [6] S. Hosokawa, J. R. Stellhorn, T. Matsushita, N. Happe, K. Kimura, K. Hayashi, Y. Ebisu, T. Ozaki, H. Ikemoto, H. Setoyama, T. Okajima, Y. Yoda, H. Ishii, Y. Liao, M. Kitaura, M. Sasaki, *Phys. Rev. B* **2017**, 96, 214207.
- [7] K. Kimura, K. Hayashi, L. V. Yashina, N. Happe, T. Nishioka, Y. Yamamoto, Y. Ebisu, T. Ozaki, S. Hosokawa, T. Matsushita, H. Tajiri, *Surf. Interface Anal.* **2019**, 51, 51.
- [8] T. Fujiwara, A. Sasahara, N. Happe, K. Kimura, K. Hayashi, H. Onishi, *Chem. Mater.* **2020**, 32, 1439.
- [9] K. Kimura, K. Yamamoto, K. Hayashi, S. Tsutsui, N. Happe, S. Yamazoe, H. Miyazaki, S. Nakagami, J. R. Stellhorn, S. Hosokawa, T. Matsushita, H. Tajiri, A. K. R. Ang, Y. Nishino, *Phys. Rev. B* **2020**, 101, 024302.
- [10] J. R. Stellhorn, Y. Ideguchi, K. Kimura, K. Hayashi, N. Happe, M. Suzuki, H. Okazaki, A. Yamashita, Y. Takano, S. Hosokawa, *Phys. Status Solidi B* **2018**, 255, 1800093.
- [11] Y. Wakabayashi, D. Nakajima, Y. Ishiguro, K. Kimura, T. Kimura, S. Tsutsui, A. Q. R. Baron, K. Hayashi, N. Happe, S. Hosokawa, K. Ohwada, S. Nakatsui, *Phys. Rev. B* **2016**, 93, 245117.
- [12] S. Hosokawa, K. Kamimura, H. Ikemoto, N. Happe, K. Mimura, K. Hayashi, K. Takahashi, K. Wakita, N. Mamedov, *Phys. Status Solidi B* **2015**, 252, 1225.
- [13] K. Hayashi, N. Uchitomi, K. Yamagami, A. Suzuki, H. Yoshizawa, J. T. Asubar, N. Happe, S. Hosokawa, *J. Appl. Phys.* **2016**, 119, 125703.
- [14] K. Fukuda, N. Kawaguchi, S. Ishizu, T. Yanagida, T. Suyama, M. Nikl, A. Yoshikawa, *Opt. Mater.* **2010**, 32, 1142.
- [15] U. Rocha, K. U. Kumar, C. Jacinto, I. Villa, F. SanzRodríguez, M. del Carmen Iglesias de la Cruz, A. Juarranz, E. Carrasco, F. C. J. M. van Veggel, E. Bovero, J. García Solé, D. Jaque, *Small* **2014**, 10, 1141.
- [16] P. Dorenbos, J. T. M. de Haas, C. W. E. van Eijk, *J. Lumin.* **1996**, 69, 229.
- [17] R. Visser, P. Dorenbos, C. W. E. van Eijk, A. Meijerink, H. W. den Hartog, *J. Phys.: Condens. Matter* **1993**, 5, 8437.
- [18] N. Abe, Y. Yokota, Y. Yanagida, N. Kawaguchi, J. Pejchal, M. Nikl, K. Fukuda, A. Yoshikawa, *IEEE Trans. Nucl. Sci.* **2010**, 57, 1278.
- [19] R. Akhmedzhanov, A. Bondartsev, V. Chernov, L. Gushchin, O. Kocharovskaya, *J. Lumin.* **2010**, 130, 1610.
- [20] Y. V. Orlovskii, H. Gross, E. E. Vinogradova, V. Boltrushko, V. Hizhnyakov, *J. Lumin.* **2020**, 219, 116920.
- [21] K. Hayashi, Y. Takahashi, E. Matsubara, S. Kishimoto, T. Mori, M. Tanaka, *Nucl. Instrum. Methods Phys. Res. B* **2002**, 196, 180.
- [22] T. Matsushita, A. Agui, A. Yoshigoe, *Europhys. Lett.* **2004**, 65, 207.
- [23] T. Matsushita, *J. Surf. Sci. Nanotech.* **2016**, 14, 158.
- [24] C. M. Bishop, *Pattern Recognition & Machine Learning*, Springer, New York **2007**.
- [25] K. Momma, F. Izumi, *J. Appl. Crystallogr.* **2011**, 44, 1272.
- [26] P. Modak, A. K. Verma, S. Ghosh, G. P. Das, *J. Phys. Chem. Solids* **2009**, 70, 922.
- [27] P. Novák, J. Kuneš, K. Knížek, *Opt. Mater.* **2014**, 37, 414.
- [28] M. Hu, Z. Zhu, Y. Wang, J. Li, Z. You, C. Tu, *Cryst. Growth Des.* **2018**, 18, 5981.
- [29] J. Růžicka, O. Caha, V. Holý, H. Steiner, V. Volobuev, A. Ney, G. Bauer, T. Duchoň, K. Veltruská, I. Khalakhan, V. Matolín, E. F. Schwier, H. Iwasawa, K. Shimada, G. Springholz, *New J. Phys.* **2015**, 17, 013028.